Drag coefficient estimation in FSI for PWR fuel assembly bowing

L. Longo, K. Cruz, E. Sarrouy, G. Ricciardi, Christophe Eloy

Drag coefficient estimation in FSI for PWR fuel assembly bowing

L. Longo[a,c,*], K. Cruz[a], N. Cadot[a], E. Sarrouy[b], G. Ricciardi[a], C. Eloy[c]

[a] *CEA, DES, IRESNE, Department of Nuclear Technology, Cadarache, 13108, Saint-Paul-Lez-Durance, France*
[b] *Aix Marseille Univ, CNRS, Centrale Marseille, LMA UMR 7031, Marseille, France*
[c] *Aix Marseille Univ, CNRS, Centrale Marseille, IRPHE, Marseille, France*

Abstract

Assembly bowing in a PWR core can be a serious problem for managing the power during normal operation or for periodical maintenance. One of the causes of this phenomenon is the transverse flow in the core, generated by the non-uniformity of the axial flow. Modelling the mechanical behaviour of a PWR core is made difficult by the complex geometry and the numerous friction points that lead to non-linearities. A simple but efficient way to deal with these issues is the porous medium model proposed by Ricciardi et al. (2009). In this model, the equations used at the fluid-structure interface require empirical parameters such as the added mass, or axial and normal drag coefficients. Using a new experimental setup at CEA, Eudore, which hosts 3 half-scale fuel assemblies in a line, the forces acting on the assembly by a non-uniform flow profile were measured. An analytical model to retrieve the normal drag coefficient was then proposed. This coefficient is then used in FSCORE, a numerical software based on the porous medium approach. The experimental and numerical results are presented and show good agreement.

Keywords: Drag coefficient, Assembly bowing, Fluid Structure interaction, LDV, PWR

*Corresponding author
Email address: lorenzo.longo@cea.fr (L. Longo)

1. Introduction

The problem of bowing in PWR assemblies has been known for some time. Andersson et al. (2005); Gabrielsson et al. (2018) describe what was the first documented case of assembly buckling in 1994 at the nuclear power plant Ringhals. In that case, the physical phenomenon was noticed after an incomplete rod insertion (IRI) accident of a control rod. The deformation of the assembly had deformed the guide thimbles, increasing friction and preventing the nominal insertion of the control rod.

During power plant maintenance, assemblies are regularly extracted and reinserted into the core. If an assembly is bowed with a C or S-shape, this operation is compromised. Andersson et al. (2005) found the largest deformation to be 20 mm, a length comparable to the nominal gap between 2 assemblies. Assembly bowing may also induce a power tilt, a common issue due to a permanent asymmetry of the power distribution (de Lambert et al., 2019). Thus, assembly bowing can be a serious problem not only to manage the power during normal operation but also during periodical maintenance.

Wanninger et al. (2018) carried out a sensitivity analysis, enlightening the different physical phenomena that can induce assembly deformation. The three most relevant phenomena are: irradiation creep, assembly growth, and hydraulic lateral forces. The authors describe the structural and material behaviour, covering the first two phenomena causing assembly bow. This paper focuses instead on the third one: lateral forces and flow redistribution. We hypothesise that lateral hydraulic forces arise mainly from inhomogeneities of the inlet flow rates. Horváth & Dressel (2013); Wanninger (2018) have analysed the flow redistribution between the inlet and the outlet and their results suggest that assembly bowing is itself a cause of lateral flows. Hence, bowing and lateral flows may amplify each other.

Modelling the mechanical behaviour of a PWR core is complicated by the complex geometry and the numerous friction points that lead to non-linear phenomena. Ricciardi et al. (2009) proposed to model a PWR core as a porous

medium, averaging over the entire core domain the structure and fluid equations. Lately de Lambert et al. (2021) proposed different 1D hydraulic models to reproduce the flow redistribution upstream from the grids for two fuel assemblies separated by a water gap that are not taken into account in the porous medium approach of Ricciardi et al. (2009) and that may be responsible for important fluid-structure interactions. On the same note, Ricciardi et al. (2022) analysed the flow on a rod array for a non-zero angle of attack. These approach that account for lateral flow can, in principle, be integrated into the porous medium approach to improve its predictions. However, the equations used at the fluid-structure interface in the porous model are empirical (Païdoussis, 2003) and they require empirical coefficients that accounts for the effect of a lateral flow. To evaluate these coefficients, Joly et al. (2018), used the 2D TLP model, based on the works of Taylor (1952); Lighthill (1960); Paidoussis (1966) and on the more recent work of Divaret et al. (2014).

Another approach to estimate these coefficients is to measure them experimentally. At the CEA in Cadarache, many experimental setups have been built in the last 30 years, with the aim of studying assemblies mechanical behaviour when interacting with the water flow. There have been full-scale (Collard et al., 2005; Ricciardi & Boccaccio, 2014) and reduced-scale setups, created to study transverse flow effect (Peybernes, 2005) or coupling between assemblies (Ricciardi et al., 2010), (Capanna et al., 2019). However, neither the flow velocity profile through the assemblies nor the hydraulic forces acting on them were measured during these experiments. The state-of-the-art setup is Eudore, a new setup hosting 3 half-scale fuel assemblies in a line. It allows us to study experimentally the effects of a flow redistribution on the assembly by measuring both the fluid forces acting on the assemblies and the flow profile. The purpose of this work is to use the experimental data of Eudore to derive, through an analytical model, the normal drag coefficient. We then use this coefficient to numerically solve the fluid-structure interaction problem with porous medium approach trying to estimate how well the simulations approximate the behaviour of the assemblies.

The paper is organised as follows. The next section introduces Eudore, enlightening its major features and how the force and velocities are measured. In section 3, an analytical model is presented to retrieve the normal drag coefficient based on the experimental data. Section 4 briefly presents the equations for the porous medium approach and the numerical data obtained with this model as well as a comparison with experimental results.

2. Experimental setup and results

Eudore is a test section that can host a row of 3 half-scale fuel assemblies under axial flow (Fig. 1). The confinement of the assemblies is 2 mm, i.e. the distance between two assemblies or between an assembly and the walls is 2 mm. Each fuel assembly consist of 60 fuel rods and 4 guide tube in a square lattice 8×8. Both the fuel rods and guide tubes are in stainless steel and their diameter is 9 mm. The height of the fuel rods is 2512 mm while the guide tubes are 82 mm longer, adding 41 mm at the bottom and at the top of the assembly. Along the height of the assembly, there are 5 spacing grids welded to the guide tube; the grids are spaced regularly along the rod length. Each grid is 101 mm width and 32 mm tall, with a plate thickness of 0.5 mm, hence lateral size of the fuel assemblies at the grids level is 101 mm, while the pin pitch is 12.5 mm. The fuel rods are trapped in the spacing grids by means of several springs. The assemblies are clamped at the bottom to the LCP (Lower Core Plate) and at the top to the UPC (Upper Core Plate). These surrogate fuel bundles have been designed for Icare facility: for a deeper description the reader is addressed to Clément (2014).

Along the test section there are 12 portholes, 4 on the frontal wall and 4 for each lateral wall of Eudore. These portholes allow us to perform non intrusive measurements on the flow velocity field using lasers and cameras. The first and the fifth grid can be considered as motionless because they are very close to the interlocking point (41 mm) as illustrated in Fig. 1a.

At height of the third grid, toolboxes can be installed in order to measure the

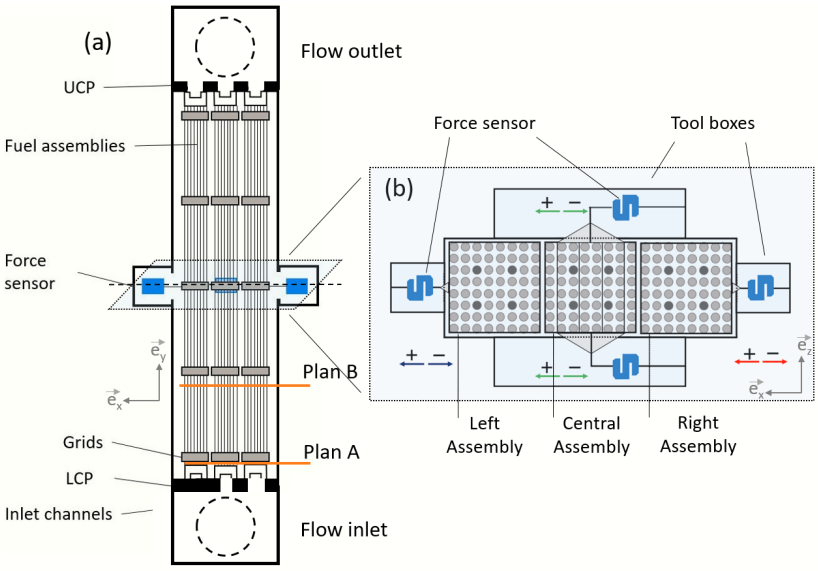

Figure 1: Eudore test section: (a) Vertical section. (b) Cross-section at the 3rd grid level; plus and minus arrows indicate the reference system of the sensors.

fluid force acting on the assemblies. The left and right assemblies are connected to the force sensors by means of preloaded pistons. If the fluid force exceeds the preload, the sensor will not be linked to the grid anymore, resulting in erroneous measurements. Therefore, the preload has to be larger than the measured force, but a preload too large will impose a significant deflection of the fuel assembly affecting the flow.

The central assembly is connected to the front and rear force sensors, "door" and "back", by means of an interlocking structure passing through the fuel rods that hooks it from side to side (Fig. 1b). These force sensors have a range of 500 N and sensibility $\sigma_s = 0.6$ N; they are stiff enough to block the assemblies' displacements. The total force on the central assembly is obtained by adding the values recorded by the "back" and "door" sensors, as they act in parallel on the central assembly.

Another feature of this setup is the possibility to change the diameter of the diaphragm located at the inlet and at the outlet of each assembly, so as to

Table 1: Diaphragm sizes per assembly.

Position	**Size**	**Left**	**Central**	**Right**
LCP	Diameter [cm]	0.00	5.65	8.00
	Area [cm^2]	0.00	25.07	50.27
UCP	Diameter [cm]	5.65	5.65	5.65
	Area [cm^2]	25.07	25.07	25.07

influence its flow. For this experiment we decided to use the set of diaphragm diameters shown in Tab. 1. The inlet diaphragms diameter grows from left to right. The outlet diaphragms are identical and equal to the diameter of the central inlet. These boundary conditions generate a transverse flow from right to left (direction $\vec{e}_x$ in Fig. 1a).

The transverse flow generated by the diaphragms exerts a force on the assemblies. By varying the flow rate, the transverse flow and therefore the force felt by the assemblies changes. The experimental campaigns allowed us to measure these forces with the force sensors, while Laser Doppler Velocimetry (LDV) allowed us to estimate the average axial and transverse components of the flow along the length of the 3 assemblies.

2.1. Force measurements

36 force experiments were performed. Among these, 10 were successful, while the others had problems during execution, e.g. too much cavitation, water leaks, inadequate piston preload, etc. The experiments were conducted varying the hydraulic pump frequency by steps of 5 Hz starting from 5 Hz. The flow rate within Eudore varies according to the pump frequency. Each flow lasted 30 s while the flow variation lasted 10 s.

Figure 2a shows how the force varies with the total flow rate. The assembly subject to most important traverse flow is always the central one. In contrast, the right assembly experiences the least transverse flow. It must be considered, however, that this assembly is the one subjected to the largest inlet flow rate;

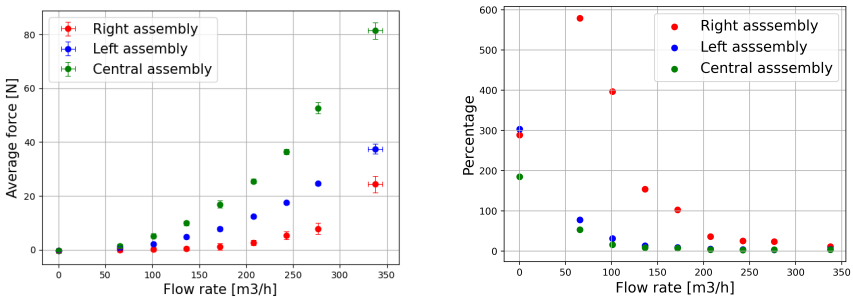

(a) Force value per assembly versus flow rate (b) Relative error per assembly versus flow rate with absolute error.

Figure 2: Force results.

its behaviour with respect to lateral flow is therefore affected by the important axial flow.

Measurement errors are calculated from the variance on the different campaigns: absolute error Δ is the square root of the sum of the measurement variance σ^2 and the quadratic value of the sensor sensibility σ_s; relative error δ is the ratio between the absolute error and the mean value $\bar{x}$.

$$\Delta = \sqrt{\sigma^2 + \sigma_s^2} \qquad \delta = \frac{\Delta}{\bar{x}} \tag{1}$$

Figure 2a shows that absolute errors are small enough to indicate a good repeatability of the experiments and hence a good reliability on the experimental data. However, the relative errors in Fig. 2b show a large uncertainty on the right assembly for low flow rates. This uncertainty could be due to an insufficient preload of the force sensor; this observation leads us to discard the right assembly data in the following analysis.

2.2. Velocimetry measurements and post-processing

First, the LDV setup is described and raw data are presented. Then, these results are post-processed in order to generate average axial and cross flows estimations along Eudore height. The latter results will be used to estimate fluid forces geometric coefficients in Sec. 3.

2.2.1. Velocimetry measurements

Laser Doppler Velocimetry (LDV) is a non-intrusive technique that uses basically a laser light and a photo detector. The measure is based on the Doppler shift on the frequency of the laser light scattered by a particle in the measurement volume. This type of application for flow velocity assumes that the flow velocity in the measurement volume has the same velocity as the particles passing through. Particles, generally on the order of 1 μm in diameter, are then dissolved in the fluid. The measurement lasts until a certain number of particles have passed through the measurement volume, of about 1 mm^3, or for a certain time limit. The result of the measurement is then a Gaussian distribution centred on the average velocity of the particles and thus of the flow velocity. For a better understanding of the LDV technique, the reader is address to Zhu (1996).

The LDV campaign was conducted at a single flow rate, 171.2 m^3/h, involving two measurement planes A and B represented in Fig. 1. Plane A is 27 mm above the bottom of the fuel rods and 13 mm before the first grid. Plane B is 505 mm above plane A, 460 mm after the first grid and 108 mm from the second grid. Each plane contains several points distributed along the horizontal section: starting from the right assembly, along the width of the experimental section, the measuring points were taken in every bypass of the first 23 rods, while in depth points are spaced 1.33 mm apart up to a depth of 50.54 mm for plane A and 65.17 mm for plane B.

Using the LDV technique, the axial velocity was measured for each point to subsequently derive the trend of the average axial velocity $V_y(x, y)$ and cross velocity $V_x(x, y)$ for each assembly. The graph in Fig. 3 is generated by taking into account the actual position of the measurement volumes. Unfortunately, the dots are too wide that they seem to form a continuous line between the rods.

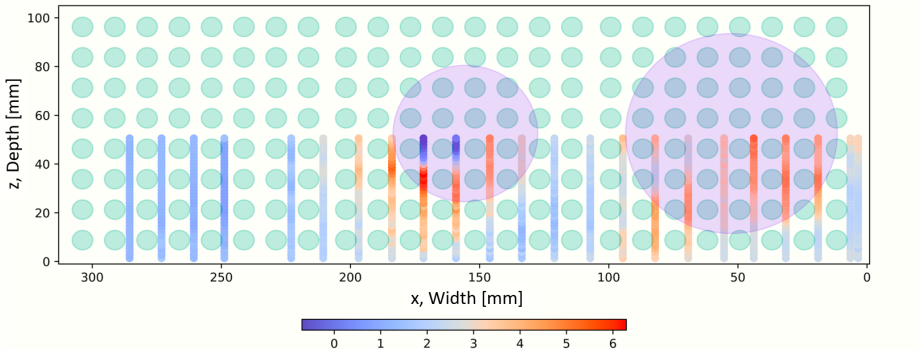

(a)

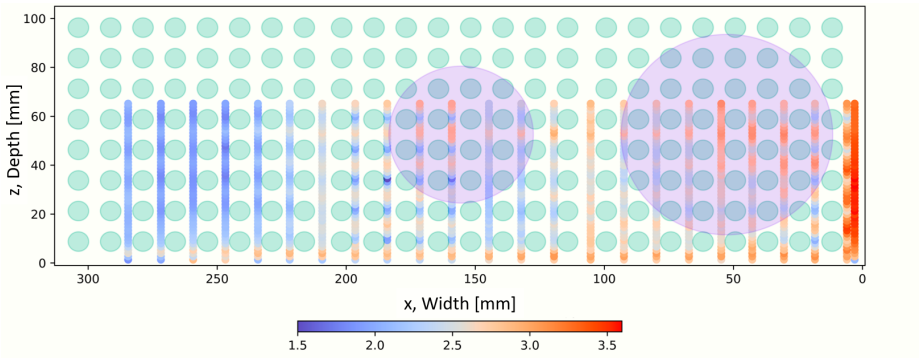

(b)

Figure 3: Measured axial velocity profiles [m/s] on planes A (a) and B (b). Blue circles represent the LCP diaphragms.

2.2.2. Measurement errors and technical issues

As previously mentioned, LDV measurements have a Gaussian trend centered on the mean velocity and whose dispersion depends on a standard deviation. Given the large number of measurement points and since our work focuses on the average flow rate per assembly more than the actual local velocity, we will simply say that for plane A we have an average standard deviation over all points of 1.05 m/s and an average velocity of 3.39 m/s, while on plane B we find an average standard deviation of 0.23 m/s for an average velocity of 2.96 m/s.

Dwelling on these numbers for a moment, we can see that the average velocity varies by about ten percentage points and that the average standard deviation is far greater in plane A than in plane B, indicating better accuracy in the latter.

As is clearly visible from Fig. 3, it should be kept in mind that the measurement points are limited in depth and width. The reasons why it was not possible to measure beyond these limits lie in the structural design of the setup: in width the limit is given by the windows width, while in depth the rear wall of Eudore reflects the laser light interfering with the measurements.

In addition to technical limitations, two drawbacks affected the measurement. On plane A, one of the front rods of the left assembly was misaligned with the others, thus obstructing the space on which the measurement could be made. Furthermore, there is a void in the centre of the second assembly surrounded by maximum velocity peaks: unfortunately a rubber gasket that fell into the hydraulic loop, got stuck right at LCP central assembly inlet channel during measurements. This causes a vortex and hence a local flow recirculation. The presence of the gasket may explain the difference in average speeds and especially the higher standard deviation on plane A. However, fortunately the gasket was in a position (central assembly inlet channel) where the flow was already turbulent and as shown in the next section, both technical limitations and problems did not have a major influence on the measurements.

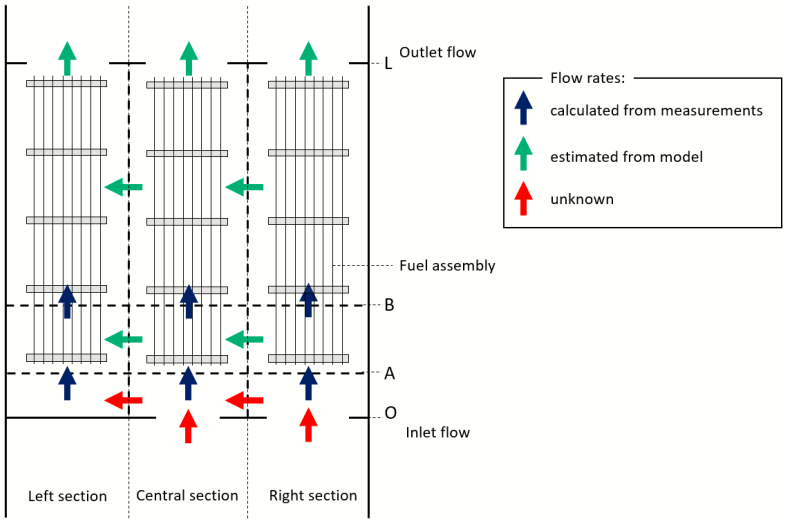

Figure 4: Axial and Transverse flow rates model.

2.2.3. Average axial and cross flows estimation

Beyond these observations, Fig. 3 shows a velocity gradient in both planes: the one in plane B is smaller, which is consistent with a more uniform flow profile as the flow develops away from the inlet, as expected.

To retrieve the full axial flow in a horizontal plane, two assumptions are needed: symmetry with respect to the vertical central axis $\vec{e}_y$ and linear extrapolation for widths greater than 285.5 mm. The total flow rate calculated with these assumptions for plane A is 178.8 m^3/h, for plane B 174.2 m^3/h while the flow rate set by the pump is 171.2 m^3/h. This good agreement shows that our assumptions are valid.

For each assembly, the mean axial flow rate along the height is estimated a polynomial interpolation of the data (Fig. 5a). A simple model is then used to estimate the transverse flows from the axial flows. Eudore section is divided into 9 sections (Fig. 4), 3 for each assembly, divided in height by 4 planes: O (Origin), A, B and L (length of the section). We do not know the exact outlet flow distribution on plane L, but in both Fig. 3 and Fig. 5 one can clearly see a rapid homogenization of flow rate within each assembly. This is primarily

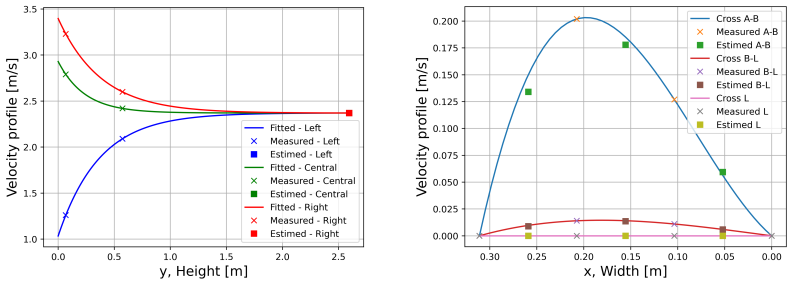

(a) V_y trend along $\vec{e}_y$

(b) V_x trend along $\vec{e}_x$

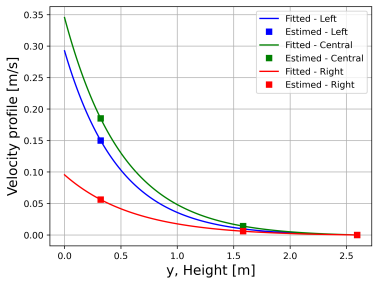

(c) V_x trend along $\vec{e}_y$

Figure 5: Axial velocity $V_y(x, y)$ and cross velocity $V_x(x, y)$ profiles estimation in Eudore for each assembly.

due to the spatial homogeneity of the volume, and the equality of the outlet diaphragms over each assembly. Therefore we can assume that the outlet flow in the plane L is identical for all the assemblies. We then use mass conservation to infer the unknown cross flow rates from the known axial flow rates.

In practice, section *right A-B* has one known flow input in plane A, one known flow output in plane B, which allows us to calculate the transverse flow towards the central assembly. This reasoning allows us to estimate the average cross flow between the three assemblies above plane A. Below, it is not possible because we do not know the inlet flow rates. Using the impermeability condition on the lateral wall and again a polynomial interpolation of the data, we can estimate the cross flow (Fig. 5bc). Axial and cross flows variations along the height can be approximated by an exponential, which shows a quick homogenisation away from the inlet.

3. Analytical model and identification of coefficients

This section proposes an analytical model, which will relate the line load $f_j(y)$ applied by the fluid on the j-th assembly to the force F_{Cj} measured by each force sensor at y_C height.

To this aim, Eudore fuel assemblies are modelled as Euler-Bernoulli beams. Each beam has 3 supports: the interlocks on the LCP and UCP that clamp both beam ends and the force sensor on the third grid which acts as a pinned condition. Hence the problem is hyperstatic and must be solved using 2 steps: first, each beam is considered as clamped at both ends receiving line load $f_j(y)$, hence implying a displacement $u_1(y)$. Then, each beam is considered as clamped at both ends and receiving a force F_{Cj} at y_C, hence implying a displacement $u_2(y)$. The line load $f_j(y)$ will be tuned such that:

$$u(y_C) = 0 \text{ whith } u(y) = u_1(y) + u_2(y). \tag{2}$$

3.1. Line load model

In our model the assemblies are 1D beams centered at half depth along $\vec{e}_z$ lying on the same plane. The symmetry of the problem allows us to reduce the space to the xy plane. The empirical model used to estimate the line load over the fuel assembly is the one proposed by Paidoussis (1966) for a cylinder submerged in an axial flow also used by Ricciardi et al. (2009). The line load model in $\vec{e}_x$ direction is then

$$\vec{f}_{\text{fluid}\to\text{A}} = 64 \times (\vec{f}_I + \vec{f}_N), \tag{3}$$

where $\vec{f}_I$ is the inertial term due to the added mass, while $\vec{f}_N$ is a force term due to the normal drag acting on one rod. With the assumption that the assembly is not moving and the flow is in stationary condition, theses contributions have the following expressions:

$$\vec{f_I} = m_f 2 V_y \frac{\partial V_x}{\partial y} \vec{e}_x = m_f f_{m_f} \vec{e}_x, \quad \vec{f_N} = \frac{1}{2} \rho d_{\text{rod}} c_N V_x V_y \vec{e}_x = c_N f_{c_N} \vec{e}_x, \quad (4)$$

where d_{rod} is the fuel rod diameter, m_f is the added mass per unit length, c_N is the normal drag coefficient, V_x is the velocity component along $\vec{e}_x$ (cross velocity), and V_y along $\vec{e}_y$ (axial velocity). The coefficients m_f and c_N depend on the geometry of the structure, its roughness, the material, and the casing. The product between the axial and transverse velocity appears in the expression of the normal drag force (Eq. 4) due to the small angle approximation proposed in Ricciardi et al. (2009). Indeed, the normal drag force is one among the normal components of the viscous forces acting on the rods in the empirical model proposed by Paidoussis (1966). In that model the only flow is axial but taking in account a small cross flow, the transverse component of the structure velocity in the expression is replaced by the transverse structure velocity relative to the fluid cross flow. The axial velocity multiplies then the transverse structure velocity relative to the fluid cross flow. Since our immobility assumption for the assembly, the transverse structure velocity is null and the cross flow velocity remains to be multiplied by the axial flow velocity. For a deeper analysis the reader is addressed to Ricciardi et al. (2009).

3.2. Displacement field under line load u_1 and punctual force u_2

Based on V_x and V_y estimations for the j-th assembly, functions f_{m_f} and f_{c_N} appearing in Eq. (4) can be evaluated. To compute the fluid force on each assembly, one needs to estimate the coefficients m_f and c_N, which are the weights for these functions in Eq. (4).

The Euler-Bernoulli equations for a clamped beam in equilibrium under a

generic load $l(y)$ are:

$$\begin{aligned} EI\partial_{yyyy}u(y) &= l(y) && \text{Static equilibrium for } y \in]0, L[, \\ u(0) &= 0 && \text{Null displacement at } y = 0, \\ \partial_y u(0) &= 0 && \text{Null section rotation at } y = 0, \\ u(L) &= 0 && \text{Null displacement at } y = L, \\ \partial_y u(L) &= 0 && \text{Null section rotation at } y = L, \end{aligned}$$

where $\partial_y u = \frac{\partial u}{\partial y}$.

When the load is the fluid force, $l(y) = m_f f_{m_f}(y) + c_N f_{c_N}(y)$ and its resolution gives a displacement $u_1(y)$:

$$u_1(y; m_f, c_N) = \frac{1}{EI}\left(m_f F^4_{m_f}(y) + c_N F^4_{c_N}(y) + \frac{a}{6}y^3 + \frac{b}{2}y^2 + cy + d\right), \quad (5)$$

where $F^4_\bullet$ denotes the fourth primitive of $f_\bullet$ ($F^4_\bullet = \int\int\int\int f_\bullet$) and the boundary conditions provide a way to determine the coefficients a, b, c and d.

When the load is the punctual force applied by a force sensor, $l(y) = F_{Cj}\delta_{y_C}$. This implies a displacement $u_2(y)$:

$$u_2(y) = \frac{1}{EI}\left(\frac{\alpha}{6}y^3 + \frac{\beta}{2}y^2 + \gamma y + \delta\right) \qquad y < y_C, \quad (6)$$

$$u_2(y) = \frac{1}{EI}\left(\frac{\alpha + F_{Cj}}{6}y^3 + \frac{\beta'}{2}y^2 + \gamma' y + \delta'\right) \qquad y \geq y_C. \quad (7)$$

Boundary conditions in conjunction with the two conditions implying equal displacement and equal section rotation at y_C allow us to determine α, β, β', γ, γ', δ and δ'.

3.3. Resolution: finding c_N from measurements

Capanna et al. (2021) used fuel assemblies of identical shape and size to those used in Eudore, albeit in larger confinement (4 mm gap between assemblies). They derived a value of the linear added mass density for an assembly $m_{f_A} = 7.78$ kg.m^{-1}, or $m_f = 0.12$ kg.m^{-1} for a single rod. To reduce the unknowns to c_N only, we use this value for m_f.

Having $u_1(y_C; c_N)$ parameterised by c_N only and $u_2(y_C)$ evaluated via the measured force, Eq. (2) can be solved, allowing us to estimate a value for c_N for each assembly. Computed values are displayed in Tab. 2 (force measurements for the right assembly were discarded as explained in Sec. 2.1).

Table 2: c_N values evaluated for left and central assemblies.

Left	**Central**	**Average**
0.48	0.84	0.66

Recently, Moussou et al. (2017) found that c_N is in the range $[0.3; 0.5]$ for a scale-one assembly. This is of the same order of magnitude than the range in Tab. 2 although our two values differ by 43%. This is surprising as the assemblies are identical in shape and material and one would expect to retrieve the same value for the normal drag coefficient c_N. This difference can be explained by the boundary conditions and the presence of the grids. The cross flow trough the central assembly encounters an homogeneous space in the $\vec{e}_x$ direction, while in the left assembly this is not valid anymore. The presence of the wall affects the velocity field, so that its gradient along $\vec{e}_x$ is larger in magnitude compared to the one in the central assembly. In Sec. 3.1 the average velocity over each assembly was used to derive the average fluid force on each rod. This approximation works better when this gradient is small, but this is not true for the lateral assemblies, which could explain the observed discrepancy on c_N.

4. Comparison with numerical simulations

Numerical simulations are implemented in EUROPLEXUS framework (abbreviated EPX, see `http://www-epx.cea.fr` for details) via a submodule named FS-CORE. EPX is a software developed for transient analyses involving nuclear reactors. FS-CORE is EPX application implementing the "porous medium" approach compatible with parallel processing. The theoretical foundations of the model are briefly recalled in the next paragraph. Faucher et al. (2021)

validated this numerical software on PWR fuel assemblies under dynamic excitation by comparing the numerical results with experiments carried out on 4 fuel assemblies geometrically identical to those of Eudore.

4.1. Porous Medium Approach

The porous medium model was developed to simulate the mechanical behaviour of an entire nuclear reactor core. The aim was to keep the number of degrees of freedom low to reduce computational costs, while accounting for the major fluid-structure interactions.

First the equations for the fluid and structure motion are established individually. Then through a porosity coefficient, equivalent fluid and structure are defined, over the whole core domain. Finally the empirical model proposed by Paidoussis (1966) is used to couple the two systems of equations.

The model starts with 5 assumptions:

- H1: The fluid is viscous, incompressible and Newtonian.
- H2: Gravity effects are neglected.
- H3: The rod section does not deform.
- H4: Distance between two rods remains constant.
- H5: Turbulent kinetic energy is negligible in comparison with turbulent diffusion.

From these 5 assumptions the model develops as summarised below. The equations of motion for the fluid are written in the ALE (Arbitrary Lagragian-Eulerian) approach, to be matched later with those for the motion of the structure written with a Lagrangian approach.

4.1.1. Equivalent fluid motion equation

The fluid is described by the Navier-Stokes equations for an incompressible fluid and neglecting gravitational effects (H1, H2). A total control volume $\Omega_t(x, y, z)$ is then defined as the union of the fluid and structure domains,

$\Omega_t(x,y,z) = \Omega_f(x,y,z) \cup \Omega_s(x,y,z)$. This control volume is centered at a point $M(x,y,z)$ and is defined with an infinitesimal square-based volume of side p and height dz, where p is the pitch between the fuel rods.

From H3 and H4 it follows that the fluid volume $V_{\Omega_f}(x,y,z)$ present in the control volume $\Omega_t(x,y,z)$ does not depend on the position M, and that the structure volume $V_{\Omega_s}(x,y,z)$ present in $\Omega_t(x,y,z)$ is equal to the one of a rod with infinitesimal height dz:

$$V_{\Omega_t}(x,y,z) = V_{\Omega_f}(x,y,z) + V_{\Omega_s}(x,y,z), \tag{8}$$

$$V_{\Omega_t}(x,y,z) = V_{\Omega_t},\ V_{\Omega_f}(x,y,z) = V_{\Omega_f} \text{ and } V_{\Omega_s}(x,y,z) = V_{\Omega_s}. \tag{9}$$

At this point the spatial averaging operation is done by integrating the Navier-Stokes equations in the fluid domain $\Omega_f(x,y,z)$, resulting in:

$$\rho \frac{1}{V_{\Omega_t}} \int_{\Omega_f(x,y,z)} \left(\frac{\partial \vec{V}}{\partial t} + \left(\vec{V} - \frac{\partial \vec{\hat{U}}}{\partial t} \right) \cdot \nabla \vec{V} \right) d\Omega = \frac{1}{V_{\Omega_t}} \int_{\Omega_f(x,y,z)} \vec{\nabla} \cdot \underline{\underline{\sigma}}_f d\Omega, \tag{10}$$

$$\frac{1}{V_{\Omega_t}} \int_{\Omega_f(x,y,z)} \vec{\nabla} \cdot \vec{V} d\Omega = 0, \tag{11}$$

where ρ is the fluid density, $\vec{V}$ is the fluid velocity, $\vec{\hat{U}}$ is a vector field that coincides with the structure displacement and, since H1, $\underline{\underline{\sigma}}_f$ is the classic Cauchy stress tensor for a Newtonian fluid whose variables are the fluid pressure P and the viscosity μ.

Ricciardi et al. (2009) chose a constant $\vec{\hat{U}}$ in the fluid domain and models turbulence by taking into account spatial fluctuations, neglecting turbulent kinetic energy (H5). The turbulent viscosity μ_T is chosen constant in space and time justified by the homogeneity of the flow of a PWR.

Finally the equivalent fluid with variables $\vec{V}_{eq}$ and P_{eq} is defined:

$$\vec{V}_{eq} = \frac{1}{V_{\Omega_f}} \int_{\Omega_f(x,y,z)} \vec{V} d\Omega, \qquad P_{eq} = \phi \frac{1}{V_{\Omega_f}} \int_{\Omega_f(x,y,z)} P d\Omega. \tag{12}$$

where $\phi = V_{\Omega_f}/V_{\Omega_t}$ is the porosity.

4.1.2. Structure model

In order to transform the 3D equilibrium equations into beam equations, the Timoshenko beam model is used. Defining ρ_s as the structure density, $\underline{\underline{\sigma}}_s$ as the Cauchy-stress tensor and $\vec{u}$ as the structure displacement, assumptions H3 and H4 lead to:

$$(1-\phi)\rho_s \frac{\partial^2}{\partial t^2}\left(\frac{1}{V_{\Omega_s}}\int_{\Omega_s(x,y,z)} \vec{u} d\Omega\right) = (1-\phi)\vec{\nabla}\cdot\left(\frac{1}{V_{\Omega_s}}\int_{\Omega_s(x,y,z)} \underline{\underline{\sigma}}_s d\Omega\right) + \underbrace{\frac{1}{V_{\Omega_t}}\int_{\partial\Omega_s(x,y,z)} \underline{\underline{\sigma}}_s \cdot \vec{n} dS}_{\vec{f}_{\text{fluid}\to\text{structure}}}. \tag{13}$$

Then the equivalent variables for structure are defined as:

$$\vec{u}_{eq} = \frac{1}{V_{\Omega_s}}\int_{\Omega_s(x,y,z)} \vec{u} d\Omega, \qquad \underline{\underline{\sigma}}_{eq} = \frac{1}{V_{\Omega_s}}\int_{\Omega_s(x,y,z)} \underline{\underline{\sigma}}_s d\Omega. \tag{14}$$

Therefore Eq. (13) is the classical Newton's law for continuous structure. Indeed, defining $\rho_{\text{seq}} = (1-\beta)\rho_s$ we have:

$$\rho_{\text{seq}} \frac{\partial^2 \vec{u}_{eq}}{\partial t^2} = (1-\phi)\vec{\nabla}\cdot\underline{\underline{\sigma}}_{eq} + \vec{f}_{\text{fluid}\to\text{structure}}. \tag{15}$$

Without going into the details of this model we will provide the system equations in the following section.

4.1.3. Coupled model

Defining the equivalent density $\rho_{eq} = \phi\rho$, the equivalent turbulent viscosity $\mu_{T_{eq}} = \phi(\mu_T + \mu)$ and the assembly mass per unit length m_A, the equations describing the coupled system are:

$$\rho_{eq}\frac{\partial \vec{V}_{eq}}{\partial t} + \rho_{eq}\nabla\cdot(\vec{V}_{eq}\otimes\vec{V}_{eq}) = -\nabla P_{eq} + \mu_{T_{eq}}\Delta\vec{V}_{eq} + 2\rho_{eq}\frac{\partial\vec{\hat{U}}}{\partial t}\cdot\nabla\vec{V}_{eq} - \rho_{eq}\vec{V}_{eq}\cdot\nabla\frac{\partial\vec{\hat{U}}}{\partial t} + \\ + \underbrace{\frac{1}{V_{\Omega_t}}\int_{\partial\Omega_s(x,y,z)}\underline{\underline{\sigma}}\vec{n}dS}_{\vec{f}_{\text{structure}\to\text{fluid}}}, \tag{16}$$

$$\nabla\cdot\vec{V}_{eq} = 0, \tag{17}$$

$$m_A\frac{\partial^2 u_{eq_x}}{\partial t^2} = \frac{\partial Q_x}{\partial y} + T_0\frac{\partial^2 u_{eq_x}}{\partial y^2} + \frac{1}{S_A}\int_{S_A}\left(f_{I_x} + f_{N_x} - yf_{L_x}\frac{\partial^2 u_{eq_x}}{\partial y^2}\right)dS, \tag{18}$$

$$m_A\frac{\partial^2 u_{eq_z}}{\partial t^2} = \frac{\partial Q_z}{\partial y} + T_0\frac{\partial^2 u_{eq_z}}{\partial y^2} + \frac{1}{S_A}\int_{S_A}\left(f_{I_z} + f_{N_z} - yf_{L_z}\frac{\partial^2 u_{eq_z}}{\partial y^2}\right)dS, \tag{19}$$

$$\vec{I}_{fA}\frac{\partial^2\vec{\theta}_{eq}}{\partial t^2} = \frac{\partial\vec{M}}{\partial x} + \vec{e}_y\wedge\vec{Q} + \vec{M}_{\text{fluid}\to\text{A}}. \tag{20}$$

$\vec{Q}$ is the shear force, $\vec{f}_L$ is the axial drag function, $\vec{T}_0$ is the tension force at the bottom of the fuel assembly, $\vec{I}_{fA}$ is the inertial moment per unit length of a fuel assembly, θ_{eq} is the section rotation and $\vec{M}$ is the bending moment. The fluid-structure interaction term $\vec{f}_{\text{structure}\to\text{fluid}}$ is integrated over the fluid-solid frontier surface $\partial\Omega_s$ and can be decomposed as follows:

$$\vec{f}_{\text{structure}\to\text{fluid}} = -\frac{1}{S_A}(\vec{f}_I + \vec{f}_N + \vec{f}_L). \tag{21}$$

$\vec{f}_L = \frac{1}{2}\rho d_{\text{rod}}c_T V_y^2\vec{e}_y$ is the lift term present in the Paidoussis model. It takes into account the axial drag and acts on the y direction. It was hence not considered it the 1D model in Section 3.1 which takes into account forces in $\vec{e}_x$ direction only. This force implies another geometric coefficient c_T. From pressure loss related experiments in Ricciardi (2020), a value $c_T = 0.02$ was determined. This value accounts for the effect of the grids on the pressure drop.

4.2. Results and discussion

The numerical simulations are performed on FS-CORE using previously estimated values for m_f, c_N and c_T. For the right assembly the c_N coefficient is

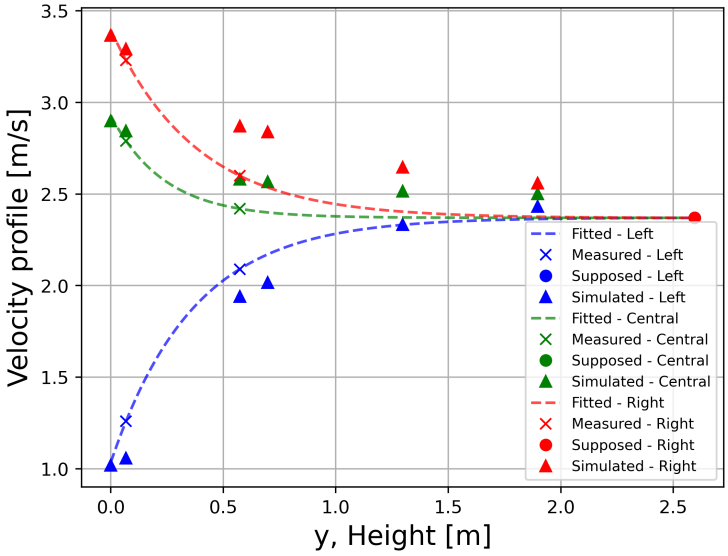

Figure 6: Axial velocity profiles [m/s] measured and simulated.

taken equal to the left one. The effect of the diaphragms is taken into account by imposing different inlet velocities for each fuel assembly based on exponential interpolation depicted in Fig. 5 at $y = 0$ obtained for a flow rate of 172 m^3/h. The ratio of axial flow rate between the fuel assemblies is kept constant for other flow rates. One would expect no axial flow at the bottom of the left fuel assembly since the diaphragm is completely closed, but the LDV measurements show a significant axial flow at that location. This is due to the possibility for the fluid to freely redistribute in the space between the lower core plate and the bottom of the fuel assemblies.

Null cross flow rate on casing walls is obtained by imposing a null cross velocity on these boundaries. Flow values are retrieved at the planes A and B level for V_y. Fig. 6 illustrates how the measured and simulated data present the same behaviour for the axial velocity field.

Using two different c_N values of Tab. 2 for laterals and central assemblies (heterogeneous set), or using the average value $c_N = 0.66$ (homogeneous set) for all the assemblies does not noticeably affect these values.

Fig. 7 shows the numerical axial and cross velocity profiles for the whole

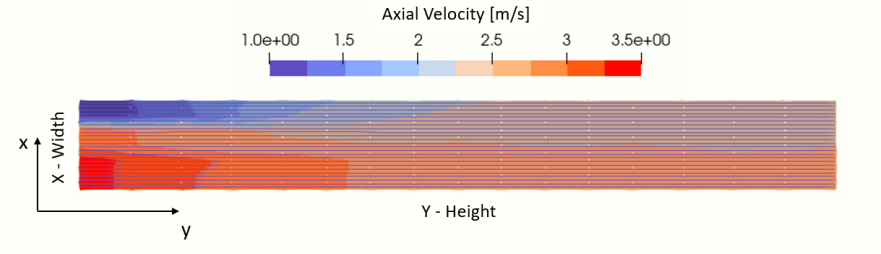

(a) Axial Velocity

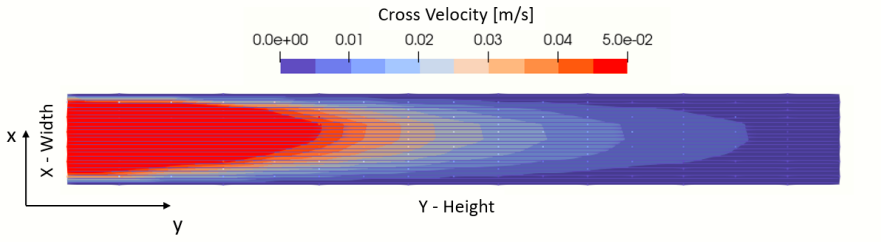

(b) Cross Velocity

Figure 7: Numerical simulation of velocity fields $V_y(x, y)$ (a) and $V_x(x, y)$ (b) for a 172 m^3/h flow and $c_N = 0.66$.

Eudore frontal section. This allows to have an idea of the velocity gradient and how it changes for each assembly. Fig. 7a shows a non homogeneous axial velocity profile at section end $y = L$. However, variations along the section width are very small, indeed the standard deviation is less than 5 %. This validates the assumptions in Sec. 2.2.3 used to derive average flow profiles. Fig. 7b exhibits a non symmetrical cross flow with respect to the section width which is consistent with experimental results depicted in Fig. 5b.

Fig. 8 compares measured and computed forces values on the third grid for both c_N values sets. Fig. 8a, 8c and 8e show data for different c_N values for lateral and central assemblies, as retrieved in Sec. 3.3. Meanwhile Fig. 8b, 8d and 8f show the numerical and experimental data with the average $c_N = 0.66$ value for the three assemblies. These results show a good agreement between numerical and experimental results in both cases with discrepancies at high flow rates for left and central assemblies. Discrepancies are observed for the

Table 3: Data differences between simulations and experiments.

	Heterogeneous c_N			Homogeneous c_N		
Assembly	Left	Central	Right	Left	Central	Right
max abs error [N]	11.99	6.04	5.58	1.79	19.94	10.40
average error [N]	3.56	3.40	3.50	1.10	4.99	5.35

right assemblies even for low flow rates, confirming the assumption of erroneous experimental data formulated in Sec. 2.1. Maxim and average absolute errors for each assembly are shown in Tab. 3 Simulations and experimental data lie on parabolic curves, so at higher flow rates one might expect more important differences. However, much higher flow rates would exceed the typical PWR velocities, hence they are beyond the interest of this paper.

A sensitivity analysis to m_f and c_N parameters was conducted via simulations. Further simulations were run using $c_N = 0.74$ for all assemblies. When compared to the results obtained for $c_N = 0.66$ that is a 12% increase, the force on the grids increase similarly (about 15%). m_f value was then increased or decreased by 17% of its original value $m_f = 0.12$. This led to a decrease (when m_f is increased) or an increase of only 2.5% of the forces exerted on the grids. This sensitivity analysis points out the importance of a correct estimate of the normal drag coefficient c_N for a proper evaluation of forces induces by cross flow and hence the bowing of the assemblies.

The differences between simulations and experiments are probably related to the presence of the grids, that are not taken into account in the numerical resolutions. The grids play a non negligible role in the flow redistribution, as shown for instance by de Lambert et al. (2021). Further experimental investigations are desirable to evaluate these effects such as measuring the pressure drop due to the presence of the grid or even adding more grids on the assemblies and measuring how the fluid forces varies with their presence.

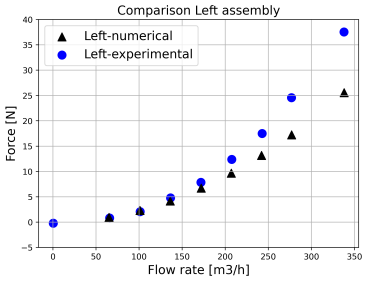

(a) Left assembly $c_N = 0.48$

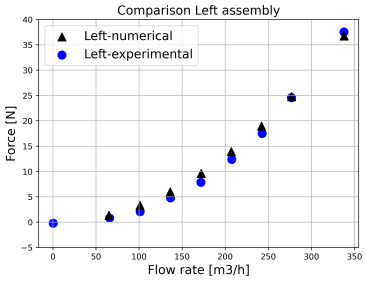

(b) Left assembly $c_N = 0.66$

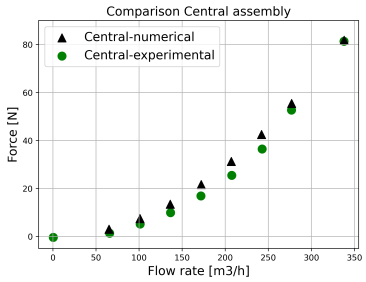

(c) Central assembly $c_N = 0.84$

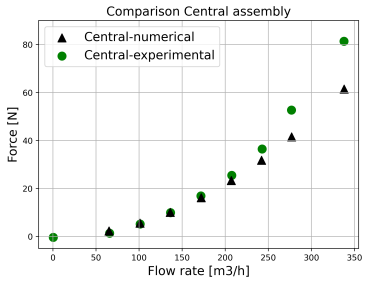

(d) Central assembly $c_N = 0.66$

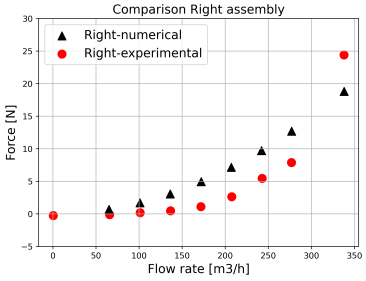

(e) Right assembly $c_N = 0.48$

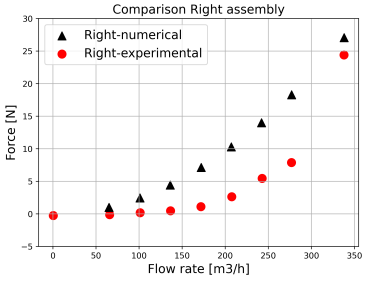

(f) Right assembly $c_N = 0.66$

Figure 8: Comparison of force values from simulations and experiments for two different sets of c_N values: left column (a,c,e) separate values for each assembly; right column (b,d,f) identical average value for all assemblies.

5. Conclusions

In this paper we have presented a study on the drag coefficient present at the basis of the fluid interaction structure for PWR fuel assemblies, which is a concern for the nuclear industry.

A new experimental set-up named Eudore which aims at studying fluid-structure interaction was presented. It involves three in line half-scale PWR assemblies and different diaphagrams at the inlet section to generate a cross flow. Instrumented with both force sensors and LDV equipments, it provided a characterization of the hydraulic forces due to a flow redistribution at different flow rates.

Based on LDV measures, average axial and flow profiles were derived for each assembly. These results were used in conjunction with an analytical model to estimate drag force coefficients. Numerical simulation based on the porous model approach showed a good agreement between experimental and numerical results as well as the great influence of the drag force coefficient on the fluid force acting on the assembly, and hence, their possible bowing.

Future experimental work will involve measurements with assemblies already bowed or free to move as well as new experiments with other types of diaphragms on the LCP or UCP. With the structure moving and the assemblies free to move, the fluid-structure interaction equations are enriched with terms regarding the velocity of the assemblies with respect to the fluid, while different diaphragms at the inlet and outlet will dictate new boundary conditions. Further investigations are desirable to evaluate the grid effect, measuring the pressure drop due to their presence or even adding more grids on the assemblies and measuring how the fluid forces varies accordingly.

Eudore offers the possibility of carrying out all these kind of experiments, i.e. it has a broad set of diaphragms, it allows flex the assemblies and even to leave them free to move and put under vibration the whole structure simulating a seismic event. It would be interesting to see how much the drag coefficient

varies with more or less transverse flow, understanding the sensibility of this investigation to the flow and to the structure conditions. This would finally shows if normal drag coefficient range of values presented in this paper can predict the force values in the assembly-wall and assembly-assembly impacts.

The setup limitations will be improved. In fact, new velocimetry campaigns involve using an opaque black slab on the rear wall of Eudore so that there are no problems with laser light reflection.

On the numerical hand, the next step will be to take into account the presence of the grids and improve the prediction on the mechanical behavior of the reactor core. Subsequently the porous medium approach can be incorporated into a multiphysics model that takes into account fission reactions, the presence of radiation and their effects on material behavior. In this way it would be possible to obtain a model that takes into account the three main phenomena responsible for the deformation of the assemblies (irradiation creep, assembly growing and hydraulic lateral forces) and that can be used in the design phase to improve the assemblies mechanical performances.

Acknowledgements

This work was developed within the framework of the MISTRAL joint research laboratory between Aix-Marseille University, CNRS, Centrale Marseille and CEA. The authors are grateful for the financial support of the Electricité de France (EDF) and FRAMATOME.

Nomenclature

ϕ	porosity coefficient		
μ	viscosity	μ_T	turbulent viscosity
$\mu_{T_{eq}}$	equivalent turbulent viscosity		
ρ	fluid density	ρ_{eq}	equivalent fluid density
$\underline{\underline{\sigma}}_f$	Cauchy stress tensor for fluid	$\underline{\underline{\sigma}}_s$	Cauchy stress tensor for structure
θ	section rotation		
Ω_f	fluid control domain	Ω_s	structure control domain
Ω_t	total control domain		
d_g	pitch	d_{rod}	fuel rod diameter
m_A	fuel assembly mass per unit length	m_f	fuel rod added mass per unit length
m_{fA}	fuel assembly added mass per unit length		
c_N	normal drag coefficient	c_T	axial drag coefficient
$\vec{f}_I$	inertial force term	f_{mf}	added mass function
$\vec{f}_N$	normal drag force term	f_{mf}	normal drag function
$\vec{f}_L$	axial drag force term	f_L	axial drag function
E	Young modulus	I	moment of inertia
L	Eudore length	M	bending moment
P_{eq}	equivalent fluid pressure	P_{fa}	pressure inside fuel assembly
Q_f	Total flow rate	Q	shear force
S	area top diaphragm	S_A	fuel assembly section
u	fuel assembly transverse displacement		
V_x	cross velocity	V_y	axial velocity
V_{Ω_f}	volume fluid control domain	V_{Ω_s}	volume structure control domain
V_{Ω_t}	volume total control domain		
W	Eudore width	W_a	fuel assembly width

References

Andersson, T., Almberger, J., & Björnkvist, L. (2005). A decade of assembly bow management at ringhals. In *Proceedings of IAEA Technical Meet-*

ing on Structural Behaviour of Fuel Assemblies for Water Cooled Reactors, Cadarache, 2004, IAEA-TECDOC (pp. 129–136). volume 1454.

Capanna, R., Ricciardi, G., Sarrouy, E., & Eloy, C. (2019). Experimental study of fluid structure interaction on fuel assemblies on the icare experimental facility. *Nuclear Engineering and Design*, *352*, 110146.

Capanna, R., Ricciardi, G., Sarrouy, E., & Eloy, C. (2021). Seismic response of cylinder assemblies in axial flow. *arXiv preprint arXiv:2110.15924*, .

Clément, S. (2014). *Mise en oeuvre expérimentale et analyse vibratoire non-linéaire d'un dispositif à quatre maquettes d'assemblages combustibles sous écoulement axial*. Ph.D. thesis Aix-Marseille.

Collard, B., Pisapia, S., Bellizzi, S., & Broc, D. (2005). Flow induced damping of a pwr fuel assembly. In *Structural behaviour of fuel assemblies for water cooled reactors: proceedings of technical meeting. Vienna* (pp. 279–288).

Divaret, L., Cadot, O., Moussou, P., & Doaré, O. (2014). Normal forces exerted upon a long cylinder oscillating in an axial flow. *Journal of Fluid Mechanics*, *752*, 649–669.

Faucher, V., Ricciardi, G., Boccaccio, R., Cruz, K., Lohez, T., & Clément, S. A. (2021). Numerical implementation and validation of a porous approach for fluid–structure interaction applied to pressurized water reactors fuel assemblies under axial water flow and dynamic excitation. *International Journal for Numerical Methods in Engineering*, *122*, 2417–2445.

Gabrielsson, P., Schrire, D., Suvdantsetseg, E., & Malmberg, M. (2018). Investigation of the development of fuel assembly bow in ringhals 3 and 4. In *Proc Int Conf Top Fuel'18*. Prague, Czech Republic.

Horváth, Á., & Dressel, B. (2013). On numerical simulation of fuel assembly bow in pressurized water reactors. *Nuclear Engineering and Design*, *265*, 814–825.

Joly, A., Badel, P., de Chassey, N. d. B., Cadot, O., Martin, A., Moussou, P., & Pastur, L. (2018). Experimental investigation of a 2-d model of fluid forces upon a cylinder array in axial flow. In *FIV2018 Conference*.

de Lambert, S., Campioni, G., Faucher, V., Leturcq, B., & Cardolaccia, J. (2019). Modeling the consequences of fuel assembly bowing on pwr core neutronics using a monte-carlo code. *Annals of Nuclear Energy*, *134*, 330–341.

de Lambert, S., Cardolaccia, J., Faucher, V., Thomine, O., Leturcq, B., & Campioni, G. (2021). Semi-analytical modeling of the flow redistribution upstream from the mixing grids in a context of nuclear fuel assembly bow. *Nuclear Engineering and Design*, *371*, 110940.

Lighthill, M. (1960). Note on the swimming of slender fish. *Journal of fluid Mechanics*, *9*, 305–317.

Moussou, P., Guilloux, A., Boccaccio, E., & Ricciardi, G. (2017). Fluid damping in fuel assemblies. In *Pressure Vessels and Piping Conference* (p. V004T04A048). American Society of Mechanical Engineers volume 57977.

Païdoussis, M. (2003). *Fluid–Structure Interactions: Slender Structures and Axial Flow.*. London: Elsevier, Academic Press.

Paidoussis, M. (1966). Dynamics of flexible slender cylinders in axial flow part 1. theory. *Journal of Fluid Mechanics*, *26*, 717–736.

Peybernes, J. (2005). Evaluation of the forces generated by cross-flow on pwr fuel assembly. *IAEA-TECDO*, *1454*, 13citation_URL_Access_Date.

Ricciardi, G. (2020). Numerical investigation of fluid forces acting on a confined cylinder with obstacle subjected to axial flow. *Science and Technology of Nuclear Installations*, *2020*.

Ricciardi, G., Bellizzi, S., Collard, B., & Cochelin, B. (2009). Modelling pressurized water reactor cores in terms of porous media. *Journal of Fluids and Structures*, *25*, 112–133.

Ricciardi, G., Bellizzi, S., Collard, B., & Cochelin, B. (2010). Fluid-structure interaction in a 3-by-3 reduced-scale fuel assembly network. *Science and Technology of Nuclear Installations*, *2010*.

Ricciardi, G., & Boccaccio, E. (2014). Measurements of fluid fluctuations around an oscillating nuclear fuel assembly. *Journal of Fluids and Structures*, *48*, 332–346.

Ricciardi, G., Peybernes, J., & Faucher, V. (2022). Analytical model of transverse pressure loss in a rod array. *Nuclear Engineering and Technology*, .

Taylor, G. I. (1952). Analysis of the swimming of long and narrow animals. *Proceedings of the Royal Society of London. Series A. Mathematical and Physical Sciences*, *214*, 158–183.

Wanninger, A. (2018). *Mechanical Analysis of the Bow Deformation of Fuel Assemblies in a Pressurized Water Reactor Core*. Ph.D. thesis Technische Universität München.

Wanninger, A., Seidl, M., & Macián-Juan, R. (2018). Mechanical analysis of the bow deformation of a row of fuel assemblies in a pwr core. *Nuclear Engineering and Technology*, *50*, 297–305.

Zhu, J. (1996). Laser doppler velocimetry for flow measurements in pulp and paper research, .